

# Atomistic Nature of Amorphous Graphite

C. Ugwumadu,<sup>\*</sup> K. Nepal, R. Thapa, and D. A. Drabold

*Department of Physics and Astronomy,  
Nanoscale and Quantum Phenomena Institute (NQPI),  
Ohio University, Athens, Ohio 45701, USA*

(Dated: August 31, 2022)

This paper focuses on the structural, electronic, and vibrational features of amorphous graphite [R. Thapa *et al.*, Phys. Rev. Lett. 128, 236402 (2022)]. The structure order in amorphous graphite is discussed and compared with graphite and amorphous carbon. The electronic density of states and localization in these phases were analyzed. Spatial projection of charge densities in the  $\pi$  bands showed a high charge concentration on participating atoms in connecting hexagons. A vibrational density of states was computed and is potentially an experimentally testable fingerprint of the material. An analysis of the vibrational modes was carried out using the phase quotient, and the mode stretching character. The average thermal conductivity calculated for aG was  $0.85 \text{ Wcm}^{-1}\text{K}^{-1}$  and  $0.96 \text{ Wcm}^{-1}\text{K}^{-1}$  at room temperature and 1000 K respectively.

## I. INTRODUCTION

The growing and unmet industrial demand for graphite, coupled with the associated environmental problems resulting from graphite mining activities have become a critical issue [1]. While the graphite feed-stock used for only lithium batteries was projected to reach an annual demand of 1.25 million tonnes by 2025 [2], the total amount of mined graphite was only 1 million tonnes in 2021 [3]. A promising method intended to mitigate the graphite supply shortage involves a "second-life" approach of graphite recycling/reuse from the spent lithium-ion batteries [4–8]. However, recent reports suggest that the environmental and economic implications of industrial-scale second-life graphite are still not favorable [9–12]. Another area of tremendous research interest is the graphitization of naturally occurring carbonaceous materials like coal [13–18]. Beyond the obvious ecological and economic benefits, the actualization of this form of modern-day alchemy would revolutionize the frontiers of science and engineering. Unfortunately, large-scale graphitization has not yet been achieved and any attempt to realize this would undoubtedly require a synergy between experiments and simulations.

It has been suspected from experiments that graphitization occurs near 3000 K, but until recently, the details of the formation process and nature of the disorder in the planes remained unknown. Our recent prediction of amorphous graphite (aG) from *ab initio* and machine learning molecular dynamic simulations suggested the possibility that the material exists [19]. We showed that carbon has an overwhelming tendency to layer, even with topological defects like 5- and 7- member rings, which fit quite naturally into the network. This discovery has fostered renewed experimental interests in the path to synthetic forms of graphite from non-crystalline carbon

structures. However, a detailed study of the atomistic nature of this carbon structure is required for significant progress in these strides.

In this paper, we elucidate the structural, electronic, and vibrational properties of aG using an ensemble of model sizes ranging from 160 - 3200 atoms. We investigated the effects of the periodic boundary conditions (PBC) in the formation process of aG and compared the atomic structure of aG to graphite and amorphous carbon. We explored the electronic structure and vibrations by computing the density of states and its corresponding inverse participation ratio. Additionally for the phonon vibrations, the phase quotient, and bond-stretching character were computed. We note here that, except stated otherwise, the analysis herein for the aG was compared with a pristine graphite model (pG) and low-density amorphous Carbon (aC) taken from references [20] and [21] respectively. Molecular dynamics calculations were done using the "Vienna *Ab initio* Simulation Package" (VASP) with plane-wave potentials [22], and the "Large-scale Atomic/Molecular Massively Parallel Simulator" (LAMMPS) [23] using the Machine-learning Gaussian Approximation Potential (ML-GAP) [24].

## II. FORMATION AND STRUCTURE

A detailed description of the simulation protocol for aG can be found in ref. [19]. In short, The aG formation process involves annealing of *ab initio* models of amorphous carbon or a random starting configuration of carbon atoms within the density range of ca.  $2.2\text{-}2.8 \text{ g/cm}^3$  in a canonical (NVT) ensemble at temperatures ranging from  $2700 \sim 4000 \text{ K}$  for up to 500 ps. The temperature was controlled using the Nosé-Hoover thermostat as implemented within VASP and LAMMPS. The animation for the aG formation process, provided in the supplementary material [25], indicates that aG is formed in a two-stage process. (1) Conversion of non- $\text{sp}^2$  into  $\text{sp}^2$  coordination. (2) The separation of the layers of  $\text{sp}^2$  atoms into amorphous graphene sheets.

<sup>\*</sup> Corresponding author.  
E-mail: cu884120@ohio.edu

The formation of aG is also dependent on the periodic boundary condition (PBC) applied. We observed that for aG, the PBC must be applied in three dimensions. It then follows that given any hexahedron with a dihedral angle of  $90^\circ$ , aG always forms if the PBC is applied within the formation density. Fig. 1 shows aG formed in a cuboid model. In another work, we reported on the formation of buckyonions from a random C network placed in a 3D vacuum, such that periodic boundary condition describes a system of isolated carbon clusters. In the same light, we found nanotubes by maintaining the PBC along the z-axis only (cylindrical symmetry) [26].

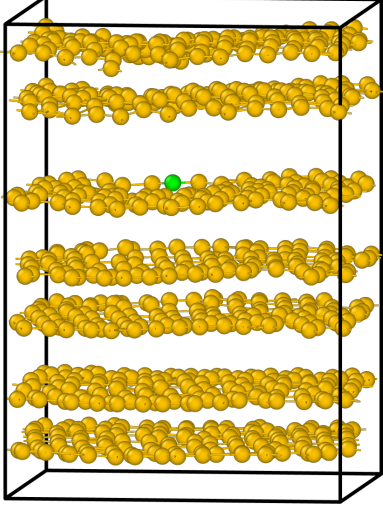


FIG. 1. aG with 520 atoms formed from an initial random C network in a cuboid. Yellow (green) represent  $sp^2$  ( $sp$ ) co-ordination.

The structural order of aG models was analyzed using pair correlation functions. Fig. 2 compares the peaks obtained for the aG models with pG and aC. The first peak for all aG was within the nearest neighbor C-C bond length observed in graphite. The aG models reproduced more graphitic peaks as the system size increased. This is a consequence of the higher ratio of hexagonal to non-hexagonal rings (6:n;  $n = 5$  or  $7$ ) found in large aG systems.

The 6:n ring ratio for the models was further confirmed from the bond angle distribution (BAD) and ring statistics. Fig. 3 shows the C-C-C angle distribution in aG<sub>3200</sub> (red), aG<sub>400</sub> (blue), and aG formed at a lower “threshold” density of  $2.0 \text{ g/cm}^3$  (green). We will henceforth refer to the aG formed at  $2.0 \text{ g/cm}^3$  as aG<sub>< $\rho$</sub> . The BAD curve for aG<sub>3200</sub> (aG<sub>400</sub>) showed a sharp (flattened) peak at  $\approx 120^\circ$ . The broad peak at  $\approx 109^\circ$  relates to non-hexagonal rings in the matrix. The ring statistics in the inset of Fig. 3 confirmed that aG<sub>3200</sub> has a higher 6:n ring ratio when compared to the other two models. Importantly, Fig. 3 (inset) indicates that the ratio of the 5- to 7- member rings (5:7) in aG<sub>400</sub> and aG<sub>< $\rho$</sub>  is equal to and greater than unity respectively. In graphite-like structures with topological defects (i.e aG), planarity is achieved only if

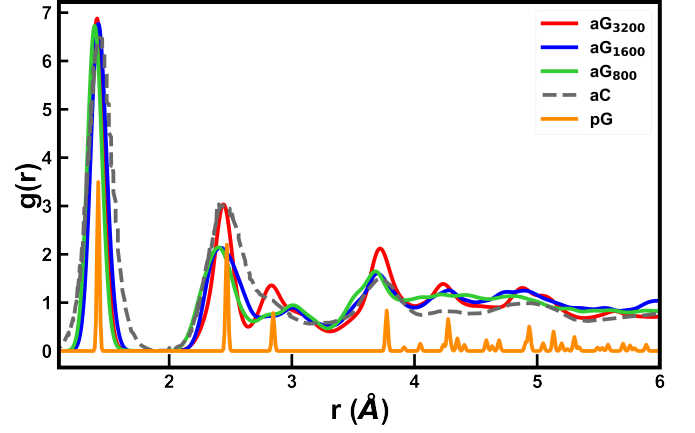


FIG. 2. Radial distribution function  $g(r)$  for different aG models compared with pG and aC

the positive curvature induced by a pentagonal ring is compensated by a negative curvature from a neighboring heptagon (or octagon) ring [27–29]. Deviation from a 1:1 ratio of pentagons and heptagons for an indeterminate number of hexagonal rings results in a complicated structure like the undulating, “worm-like” layers seen in aG<sub>< $\rho$</sub>  (see Fig. 4 [TOP]), as opposed to “almost” flat layers observed in aG within the desired density (see Fig. 4 [BOTTOM]).

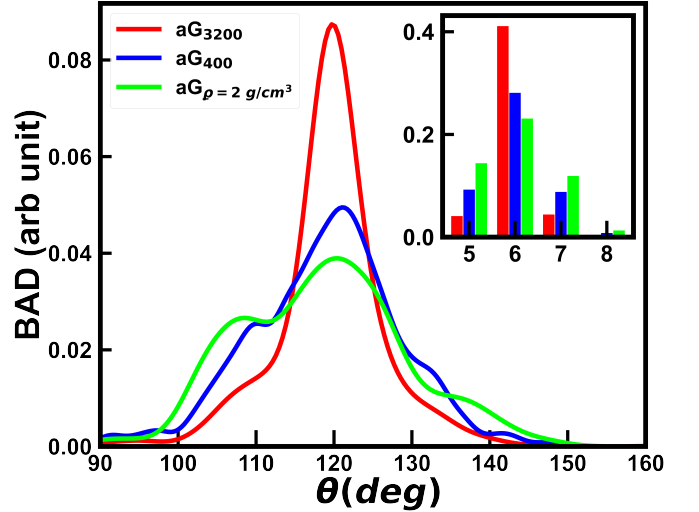


FIG. 3. Bond angle distribution (BAD) analysis and ring statistics (inset) for aG<sub>3200</sub> (red), aG<sub>400</sub> (blue) and a 160-atom aG model with a density of  $2 \text{ g/cm}^3$  (green). The distribution has been smoothed to clearly show the peaks

Next, we analyzed the local conformation and coordination number ( $N$ ) of the aG models by implementing an *ab initio* multiple scattering calculations of the extended x-ray absorption fine structure (EXAFS) using the real-space Green’s function code FEFF10 [30] for the K-edge. Using the Kaiser windowing function, with  $\beta = 2$  [31], the extracted post-edge oscillations ( $\chi(E)$ ) were Fourier

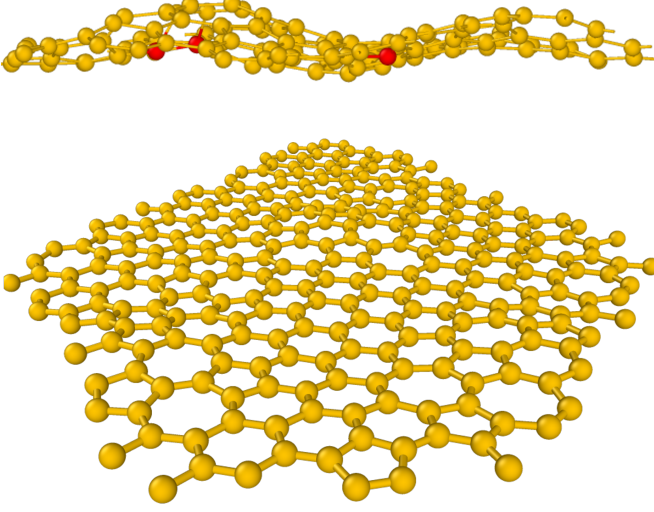


FIG. 4. Figure showing a representative layer for [TOP] the undulating (worm-like) structure ( $\rho = 2 \text{ g/cm}^3$ ) and [BOT-TOM] flat structure for aG formed below and within the desired density ( $\rho = 2.44 \text{ g/cm}^3$ ) respectively. Yellow (red) represents three-fold (four-fold) coordination.

transformed (FT) into frequency space, and the resulting spectrum gives the radial distribution function (RDF). Fig. 5 compares the normalized Fourier amplitude acquired for aG<sub>1600</sub> and pG. All the peaks in aG<sub>1600</sub> corresponded with some peaks in pG. The first peak at 0.134 nm is due to the first-neighbor C-C scattering (0.142 nm,  $N = 3$ ) [32]. The second (0.243 nm,  $N = 6$ ) and third (0.281 nm,  $N = 3$ ) peaks in pG were resolved as a single second peak in aG at 0.243 nm. This "second peak" in aG has been identified in low-density amorphous carbon by Bhattarai and co-workers [21]. Unlike pG, the aG model did not produce additional peaks beyond the fourth C-C scattering peak at 0.38 nm, and this suggests an intermediate-range order in aG. We note here that the FT peaks calculated for pG are consistent with those published in literature [32–34] and the results for aG are in agreement with the pair correlation function calculations in Fig. 2. This presents a prediction to be employed with experiments.

### III. ELECTRONIC STRUCTURE

The electronic density of states (EDoS) for aG was computed within VASP and the extent of localization of Kohn-Sham states ( $\phi$ ) was calculated as the participation ratio (EIPR) using the following equation:

$$I(\phi_n) = \frac{\sum_i |a_n^i|^4}{(\sum_i |a_n^i|^2)^2} \quad (1)$$

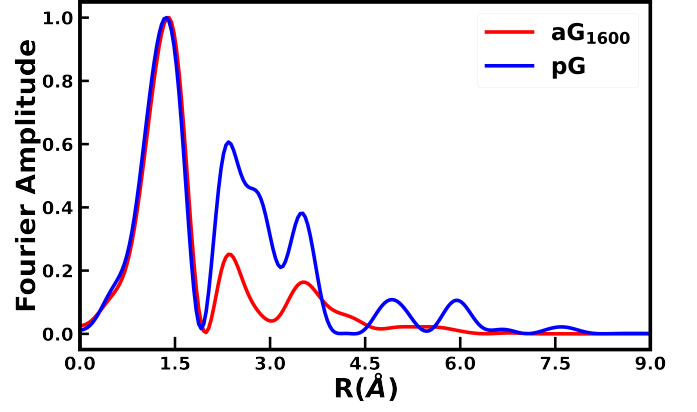


FIG. 5. Normalized Fourier amplitude for the C K-edge EXAFS spectra for pG and aG<sub>1600</sub>.

where  $a_n^i$  is the contribution to the eigenvector ( $\phi_n$ ) from the  $i^{\text{th}}$  atomic orbital. High (low) values of EIPR indicate localized (extended) states.

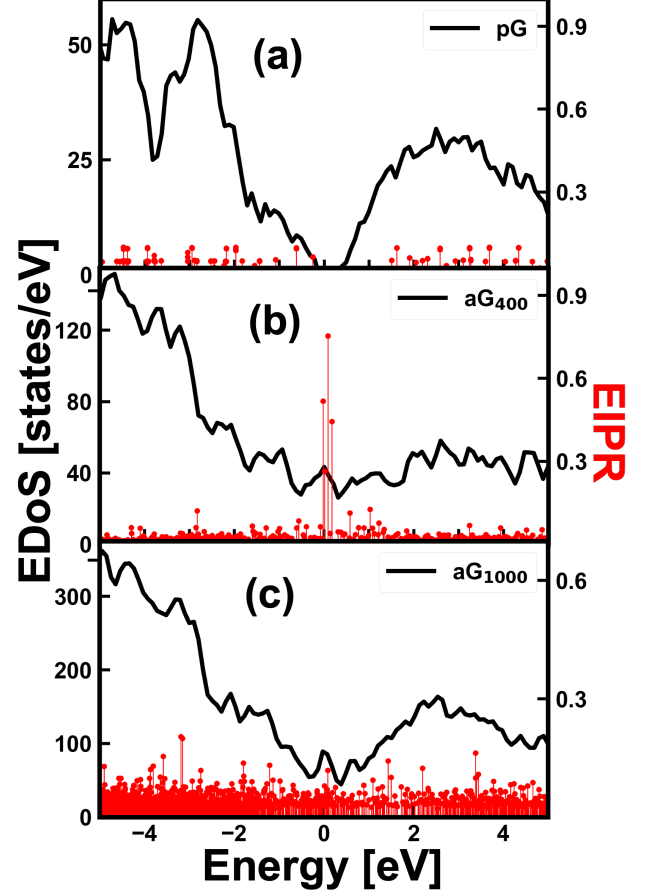


FIG. 6. Electronic DoS and IPR for pG and some aG models.

The EDoS and EIPR for pG, aG<sub>400</sub> and aG<sub>1000</sub> are shown in Fig. 6 (a-c) with the Fermi-level ( $E_f$ ) shifted to zero. Fig. 6 (a) depicts an expected gap at  $E_f$  in pG, with low

IPR values for states in the conduction and valence region [35]. On the other hand, aG does not show any gap at  $E_f$ , and some states are localized (see 6 (b and c)). The states with the highest EIPR values were predominantly distributed among non-hexagonal rings in the matrix as shown in Fig. 7.

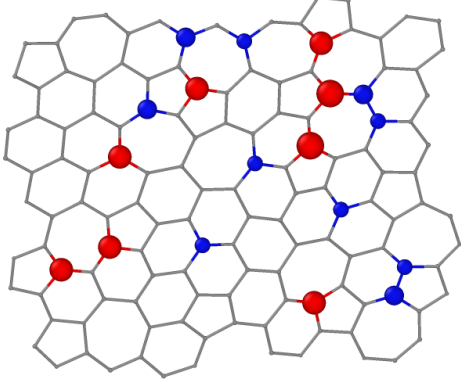


FIG. 7. Spatial projection of localized states near  $E_f$  on the atoms in aG<sub>400</sub>. Red- and blue-colored spheres represent the two highly localized states.

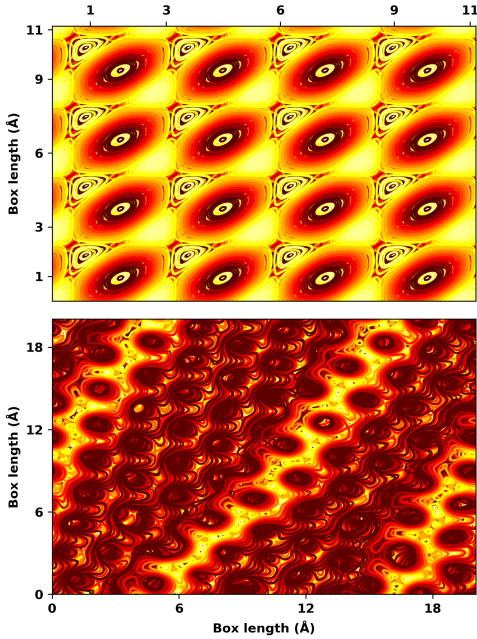


FIG. 8. The charge density distribution projected on planes of pG [TOP] compared to that of aG<sub>1000</sub> [BOTTOM]. Only the  $\pi$  orbitals are considered. The charge density is enhanced on connected hexagonal paths.

In ref. [19], using the space-projected conductivity (SPC) formalism [36], we showed that the conduction-active path in aG was exclusively along connecting atoms in hexagonal rings. To further analyze this, We projected the laterally averaged charge density for the  $\pi$  orbitals onto the planes of atoms. Our result, presented as a con-

tour heat-map plot in Fig. 8, revealed that the regions with the highest values are on the planes with highly connecting hexagonal rings. This is consistent with our initial findings from the SPC calculation and also suggests that, even with the topological disorder in its layers, to some extent, aG possesses a degree of order in the way the electrons interact in-plane ( $\sigma$  electrons) and out-of-plane ( $\pi$  electrons).

#### IV. VIBRATIONS

Thermal and mechanical properties, as well as the local bonding environment, can be obtained from the vibrations of amorphous materials. The harmonic approximation for vibrations requires evaluating the Hessian matrix, which is accomplished by force calculation from 0.015 Å atomic displacements in six directions ( $\pm x, \pm y, \pm z$ ). The vibrational density of states (VDoS) is calculated as:

$$g(\omega) = \frac{1}{3N} \sum_{i=1}^{3N} \delta(\omega - \omega_i) \quad (2)$$

where,  $N$  and  $\omega_i$  represent the number of atoms and the eigen-frequencies of normal modes, respectively. The delta function (approximated by a Gaussian with a standard deviation equal to 1.5% the maximum frequency) ensures that high-density values were assigned to vibration frequencies that lie close to the normal modes. The extent of localization of each normal mode frequency was calculated through the vibration inverse participation ratio (VIPR), defined as:

$$V(\omega_n) = \frac{\sum_{i=1}^N |\mathbf{u}_n^i|^4}{(\sum_{i=1}^N |\mathbf{u}_n^i|^2)^2} \quad (3)$$

where,  $\mathbf{u}_n^i$  is displacement vector of  $i^{th}$  atom at normal mode frequency  $\omega_n$ . By definition, low values of VIPR indicate vibrational mode evenly distributed among the atoms while higher values imply that few atoms contribute at that particular eigen-frequency.

Fig. 9 shows the total VDoS for amorphous and pristine graphite [TOP] and the extent of localization from the VIPR [BOTTOM]. While the peaks for aG and pG do not match, the overall shape of both models remained consistent. The figure also provides a vibrational fingerprint of aG to be examined in experiments. The VIPR for aG suggests that more states are localized in the high-frequency region which corresponds to the “optical” mode. The classification of phonon vibrations into pure acoustic and optical modes cannot be rigorously applied for non-crystals due to the lack of periodicity in the lattice, which restricts vibrations to non-propagating modes (e.g. diffusons and locons) [37, 38]. However, the phase quotient ( $Q_p$ ) of Bell and Hibbins-Butler [39] provides a



measure of how vibrations of neighboring atoms are in-phase (acoustic mode) and out-of-phase (optical mode). The normalized  $Q_p$  is given as [40]:

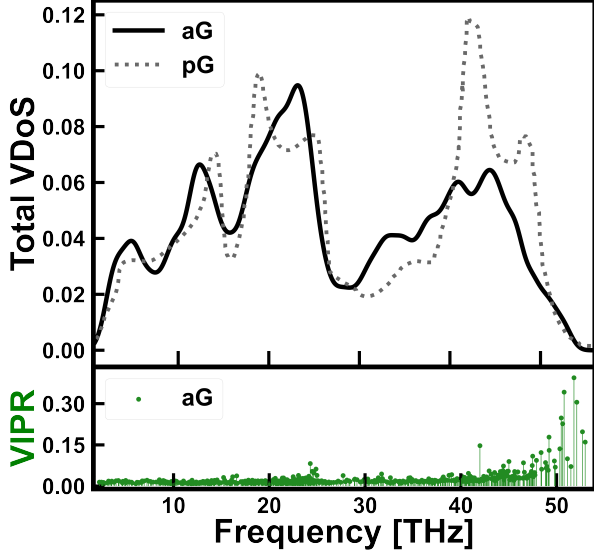


FIG. 9. [TOP] The total VDoS for amorphous and pristine graphite calculated from the harmonic approximation as implemented within VASP. [BOTTOM] VIPR amorphous Graphite.

$$Q_p = \frac{1}{N_b} \frac{\sum_m \mathbf{u}_p^i \cdot \mathbf{u}_p^j}{\sum_m |\mathbf{u}_p^i \cdot \mathbf{u}_p^j|} \quad (4)$$

where  $N_b$  is the number of valance bonds,  $\mathbf{u}_p^i$  and  $\mathbf{u}_p^j$  are the normalized displacement vectors (see Eq. 3) for the  $p^{th}$  normal mode. The index,  $i$ , sums over all the C atoms and  $j$  enumerates neighboring atoms of the  $i^{th}$  atom. The vibration of the bulk material in unison gives  $Q_p = 1$  (purely acoustic). Conversely, a value of -1 would correspond to motion in the opposite direction between neighboring atoms (purely optical). It then follows that positive (negative)  $Q_p$  is more “acoustic-like” (“optical-like”). However near 0, one cannot necessarily distinguish between acoustic and optical modes. The phase quotient for aG<sub>400</sub> is plotted in Fig 10 [LEFT]. The dashed line identifies the diffusion to locon transition level, which is conceptually the region where VIPR  $\gtrsim 0.15$  [41]. It then follows that the  $Q_p$  has high negative values at the high-frequency end of the spectrum and frequencies below the dotted line are locons. However, vibrational modes around the inflection point at  $\approx 23$  THz are not locons, but can be considered as quasi-localized “Resonant modes”. This results from the finite size of the supercell and diffuses away for larger systems [42]. The animation for vibration at one of the Resonant mode frequencies (see quasiLocalized.freq.mp4 in the supplementary material [25]) confirms that the normal modes are not truly localized but rather majorly distributed amongst C atoms at the boundaries.

We further investigated the vibration modes by calculating the bond-stretching character ( $S(\omega)$ ) of aG using the following equation:

$$S(\omega) = \frac{\sum_m |\mathbf{u}_n^i - \mathbf{u}_n^j| \times \hat{\mathbf{r}}_{ij}}{\sum_m |\mathbf{u}_n^i - \mathbf{u}_n^j|} \quad (5)$$

$\mathbf{u}_n^i$  and  $\mathbf{u}_n^j$  are as defined in Eqn. 3,  $\hat{\mathbf{r}}_{ij}$  is the unit vector parallel to the  $m^{th}$  bond.  $S(\omega)$  is close to unity when the mode of vibration is predominantly of bond-stretching type and will be close to 0 otherwise. The Vibrations in aG were observed to be in-plane (out-of-plane) at high (low) frequencies, which are similar to what is found in pristine graphite [43, 44]. The in-plane vibrations involve the stretching of C-C bonds of neighboring atoms, while the out-of-plane vibrations correspond to the breathing mode of individual layers in aG [45, 46]. Fig. 10 shows that bond stretching in the planes is dominant at high frequencies. We have included two animations in the supplementary material showing the stretching character and breathing mode at the extremes of the frequency spectrum [25]. It is noteworthy that at the mid-spectrum (see quasiLocalized.freq.mp4 [25]), there is a combination of both characteristics as predicted from the phase quotient.

We point out that beyond the basic classification of vibrational modes in aG, the optical-like modes (negative  $Q_p$  with the bond-stretching character) contribute to the thermal conductivity in disordered systems. This has been reported for amorphous carbon in the work of Hamid and coworkers [47], where they found that at high temperatures (with heat capacity satisfying the Dulong-Petit limit), vibration regions with negative  $Q_p$  contribute as much as 40 % to the total thermal conductivity. Using LAMMPS, we analyzed the contribution of the topological defect to the thermal conductivity (TC) in aG<sub>540</sub>. The contribution of the heat flux ( $\mathbf{J}$ ) for each atom [48, 49] was calculated, and then an ensemble average of the auto-correlation of  $\mathbf{J}$  was related to the TC ( $\kappa$ ) using the equilibrium Green-Kubo formalism given as [50, 51]:

$$\kappa = \frac{1}{3VK_B T^2} \int_0^\tau \langle \mathbf{J}(0) \cdot \mathbf{J}(t) \rangle dt \quad (6)$$

where  $V$ ,  $T$ , and  $K_B$  are the system volume, temperature, and Boltzmann’s constant, respectively. The upper limit of the integral was approximated by  $\tau$  ( $= 0.5$  ns) which is the correlation time required for the heat current autocorrelation to decay to zero. The TC was obtained by averaging the integral in Eq. 6 from 5 independent microcanonical ensembles. The Nosé–Hoover thermostat [52, 53] was used for thermalization and equilibration at  $T = 300$  K and 1000 K in a fixed volume using a 1 fs time-step. At the beginning of the simulation, initial velocities were assigned to the atoms randomly from a Gaussian distribution. Our result showed that the average TC calculated for aG was  $0.85 \text{ Wcm}^{-1}\text{K}^{-1}$  and  $0.96$

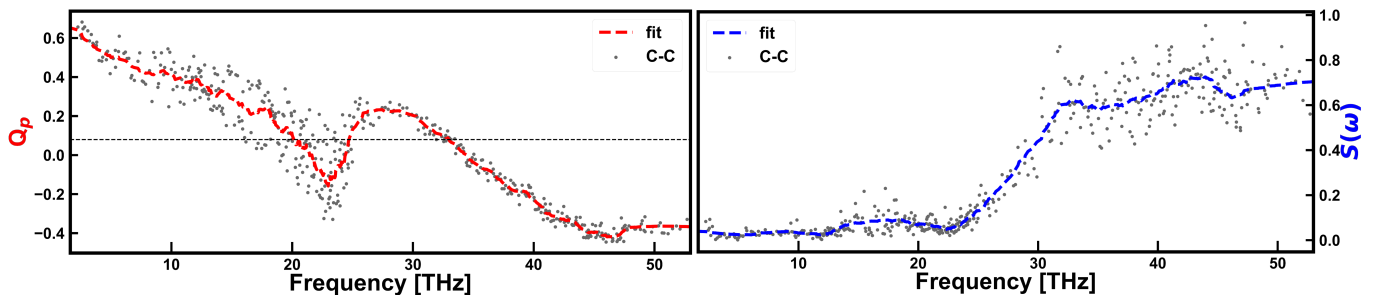


FIG. 10. Figure showing the [LEFT] phase quotient and [RIGHT] stretching character of aG. The dashed line shows the level at which VIPR = 0.15

$\text{Wcm}^{-1}\text{K}^{-1}$  at 300 K and 1000 K respectively. The increase in the thermal conductivity is consistent with what is observed for amorphous systems like aC and amorphous silicon [47, 54, 55]. We note that the room temperature TC of aG is  $\approx 5\%$  of that of pyrolytic graphite ( $\kappa \approx 19.5 \text{ Wcm}^{-1}\text{K}^{-1}$ ) [55]. However, the 11 % increase for aG at 1000 K, compared to the  $\approx 73\%$  decrease for pyrolytic graphite [55] at the same temperature, could be important for applications.

## V. CONCLUSION

This work focused on the structural, electronic, and vibration properties of amorphous graphite (aG). aG formed only with PBC in all dimensions within the density range of ca.  $2.2\text{--}2.8 \text{ g/cm}^3$ . However, at a "threshold" density of  $2.0 \text{ g/cm}^3$ , an undulating layered structure was observed. Structural features were analyzed and compared to pristine graphite by exploiting the radial distribution function and coordination number. Electronic structure analysis showed that there was no band-gap at the Fermi-level in aG. few states were observed to

be localized on 5- and 7-member rings in the layers. Spatial projection of the charge density near the Fermi-level ( $\pi$  orbitals) showed high values on connecting 6-member rings. The density of state and corresponding participation ratio for the phonon vibrations were analyzed, and the result showed that aG has more states localized at the high-frequency end of the vibration spectrum. phase quotient and stretching character analysis further suggested that those localized sites were from atoms participating in non-hexagonal rings. The average thermal conductivity for aG was calculated at room temperature ( $0.85 \text{ Wcm}^{-1}\text{K}^{-1}$ ) and 1000 K ( $0.96 \text{ Wcm}^{-1}\text{K}^{-1}$ ) indicated an 11 % increase in thermal conductivity.

## ACKNOWLEDGMENTS

We thank XSEDE (supported by National Science Foundation Grant No. ACI-1548562) for computational support under allocation no. DMR-190008P.

The Figures 4, 1 and 7 were made using the Open-Visualization Tool (OVITO) [56]. All the animations were made using Jmol [57].

- [1] D. Olson, R. Virta, M. Mahdavi, E. Sangine, and S. Fortier, Natural graphite demand and supply—implications for electric vehicle battery requirements, *The Geological Society of America* **520**, 67 (2016).
- [2] R. Mills, Graphite deficit starting this year, as demand for EV battery anode ingredient exceeds supply, <https://www.mining.com/web/graphite-deficit-starting-this-year-as-demand-for-ev-battery-anode-ingredient-exceeds-supply> Accessed: 2022-08-03.
- [3] U.S. Geological Survey, Mineral Commodity Summaries, 2022-Graphite, <https://pubs.usgs.gov/periodicals/mcs2022/mcs2022-graphite.pdf>, accessed: 2022-06-25.
- [4] Y. Gao, C. Wang, J. Zhang, Q. Jing, B. Ma, Y. Chen, and W. Zhang, Graphite recycling from the spent lithium-ion batteries by sulfuric acid curing-leaching combined with high-temperature calcination, *ACS Sustainable Chemistry & Engineering* **8**, 9447 (2020).
- [5] D. Liu, X. Qu, B. Zhang, J. Zhao, H. Xie, and H. Yin, Alkaline roasting approach to reclaiming lithium and graphite from spent lithium-ion batteries, *ACS Sustainable Chemistry & Engineering* **10**, 5739 (2022).
- [6] M. Bhar, S. Ghosh, S. Krishnamurthy, K. Yalaman-chili, and S. K. Martha, Electrochemical compatibility of graphite anode from spent li-ion batteries: Recycled via a greener and sustainable approach, *ACS Sustainable Chemistry & Engineering* **10**, 7515 (2022).
- [7] S. Natarajan, K. Krishnamoorthy, A. Sathyaseelan, V. K. Mariappan, P. Pazhamalai, S. Manoharan, and S.-J. Kim, A new route for the recycling of spent lithium-ion batteries towards advanced energy storage, conversion, and harvesting systems, *Nano Energy* **101**, 107595 (2022).
- [8] C. Yi, P. Ge, X. Wu, W. Sun, and Y. Yang, Tailoring carbon chains for repairing graphite from spent lithium-ion battery toward closed-circuit recycling, *Journal of Energy Chemistry* **72**, 97 (2022).
- [9] A. P. Velenturf and P. Purnell, Principles for a sustainable circular economy, *Sustainable Production and Con-*

- sumption **27**, 1437 (2021).
- [10] I. Rey, C. Vallejo, G. Santiago, M. Iturrondobeitia, and E. Lizundia, Environmental impacts of graphite recycling from spent lithium-ion batteries based on life cycle assessment, *ACS Sustainable Chemistry & Engineering* **9**, 14488 (2021).
  - [11] N. Niese, C. Pieper, A. Arora, , and A. Xie, The Case for a Circular Economy in Electric Vehicle Batteries, <https://www.bcg.com/publications/2020/case-for-circular-economy-in-electric-vehicle-batteries> Accessed: 2022-08-07.
  - [12] Pham, Thi Thuy Linh, The second life - Challenges of repurposing electric vehicle lithium-ion batteries (2021), The International Institute for Industrial Environmental Economics Master Thesis.
  - [13] C. A. Masi, T. A. Schumacher, J. Hilman, R. Dulal, G. Rimal, B. Xu, B. Leonard, J. Tang, M. Fan, and T. Chien, Converting raw coal powder into polycrystalline nano-graphite by metal-assisted microwave treatment, *Nano-Structures and Nano-Objects* **25**, 100660 (2021).
  - [14] T. Qiu, J.-G. Yang, and X.-J. Bai, Preparation of coal-based graphite with different microstructures by adjusting the content of ash and volatile matter in raw coal, *Energy Sources, Part A: Recovery, Utilization, and Environmental Effects* **42**, 1874 (2020), <https://doi.org/10.1080/15567036.2019.1604900>.
  - [15] H. Marsh and F. Rodríguez-Reinoso, Chapter 9 - production and reference material, in *Activated Carbon*, edited by H. Marsh and F. Rodríguez-Reinoso (Elsevier Science Ltd, Oxford, 2006) pp. 454–508.
  - [16] T. Qiu, Z. Yu, W. Xie, Y. He, H. Wang, and T. Zhang, Preparation of onion-like synthetic graphite with a hierarchical pore structure from anthracite and its electrochemical properties as the anode material of lithium-ion batteries, *Energy & Fuels* **36**, 8256 (2022), <https://doi.org/10.1021/acs.energyfuels.2c01892>.
  - [17] Z. Adamczyk, J. Komorek, B. Białecka, J. Moszko, and A. Klupa, Possibilities of graphitization of unburned carbon from coal fly ash, *Minerals* **11**, 1027 (2021).
  - [18] Y. Wu, K. Li, Z. Wang, M. Hu, H. Cao, and Q. Liu, Fluctuations in graphitization of coal seam-derived natural graphite upon approaching the qitianling granite intrusion, hunan, china, *Minerals* **11**, 10.3390/min11101147 (2021).
  - [19] R. Thapa, C. Ugwumadu, K. Nepal, J. Trembly, and D. A. Drabold, Ab initio simulation of amorphous graphite, *Phys. Rev. Lett.* **128**, 236402 (2022).
  - [20] R. Wyckoff, *Crystal Structures*, Crystal Structures No. v. 1 (Interscience Publishers, 1963).
  - [21] B. Bhattarai, P. Biswas, R. Atta-Fynn, and D. A. Drabold, Amorphous graphene: a constituent part of low density amorphous carbon, *Phys. Chem. Chem. Phys.* **20**, 19546 (2018).
  - [22] G. Kresse and J. Furthmüller, Efficient iterative schemes for ab initio total-energy calculations using a plane-wave basis set, *Phys. Rev. B* **54**, 11169 (1996).
  - [23] A. P. Thompson, H. M. Aktulga, R. Berger, D. S. Bolintineanu, W. M. Brown, P. S. Crozier, P. J. in 't Veld, A. Kohlmeyer, S. G. Moore, T. D. Nguyen, R. Shan, M. J. Stevens, J. Tranchida, C. Trott, and S. J. Plimpton, LAMMPS - a flexible simulation tool for particle-based materials modeling at the atomic, meso, and continuum scales, *Computer Physics Communications* **271**, 108171 (2022).
  - [24] V. L. Deringer and G. Csányi, Machine learning based interatomic potential for amorphous carbon, *Phys. Rev. B* **95**, 094203 (2017).
  - [25] Supplemental materials with animation showing the formation of aG and its different phonon vibration modes.
  - [26] C. Ugwumadu, K. Nepal, R. Thapa, Y. G. Lee, Y. A. Majali, J. Trembly, and D. A. Drabold, Simulation of multi-shell fullerenes using machine-learning Gaussian Approximation Potential, submitted to Carbon Trends on 08/2022. Available at SSRN: <http://dx.doi.org/10.2139/ssrn.4200272>.
  - [27] A. L. Mackay and H. Terrones, Diamond from graphite, *Nature* **352**, 762 (1991).
  - [28] H. Terrones and A. Mackay, Hypothetical curved graphite, *Nanostructured Materials* **3**, 319 (1993), proceedings of the First International Conference on Nanos-structured Materials.
  - [29] T. Lenosky, X. Gonze, M. Teter, and V. Elser, Energetics of negatively curved graphitic carbon, *Nature* **355**, 333 (1992).
  - [30] J. J. Kas, F. D. Vila, J. J. Rehr, C. D. Pemmaraju, and T. S. Tan, *Advanced calculations of x-ray spectroscopies with feff10 and corvus* (2021).
  - [31] J. F. Kaiser, *Digital Filters” - Ch 7 in Systems analysis by digital computer* (John Wiley and Sons, New York, 1966) pp. 218–285.
  - [32] G. Comelli, J. Stöhr, W. Jark, and B. B. Pate, Extended x-ray-absorption fine-structure studies of diamond and graphite, *Phys. Rev. B* **37**, 4383 (1988).
  - [33] T. Tanaka, N. Matsubayashi, M. Imamura, and H. Shimada, Synchronous scanning of undulator gap and monochromator for XAFS measurement in soft X-ray region, *Journal of Synchrotron Radiation* **8**, 345 (2001).
  - [34] B. Buades, D. Moonshiram, T. P. H. Sidiropoulos, I. León, P. Schmidt, I. Pi, N. D. Palo, S. L. Cousin, A. Picón, F. Koppens, and J. Biegert, Dispersive soft x-ray absorption fine-structure spectroscopy in graphite with an attosecond pulse, *Optica* **5**, 502 (2018).
  - [35] D. A. Drabold, P. Ordejón, J. Dong, and R. M. Martin, Spectral properties of large fullerenes: From cluster to crystal, *Solid State Communications* **96**, 833 (1995).
  - [36] K. Prasai, K. N. Subedi, K. Ferris, P. Biswas, and D. A. Drabold, Spatial Projection of Electronic Conductivity: The Example of Conducting Bridge Memory Materials, *physica status solidi (RRL) – Rapid Research Letters* **12**, 1800238 (2018).
  - [37] P. B. Allen and J. L. Feldman, Thermal conductivity of disordered harmonic solids, *Phys. Rev. B* **48**, 12581 (1993).
  - [38] P. B. Allen, J. L. Feldman, J. Fabian, and F. Wooten, Diffusons, locons and propagons: Character of atomic vibrations in amorphous si, *Philosophical Magazine B* **79**, 1715 (1999).
  - [39] R. J. Bell and D. C. Hibbins-Butler, Acoustic and optical modes in vitreous silica, germania and beryllium fluoride, *Journal of Physics C: Solid State Physics* **8**, 787 (1975).
  - [40] P. B. Allen, J. L. Feldman, J. Fabian, and F. Wooten, Diffusons, locons and propagons: Character of atomic vibrations in amorphous si, *Philosophical Magazine B* **79**, 1715 (1999), <https://doi.org/10.1080/13642819908223054>.
  - [41] H. R. Seyf, L. Yates, T. L. Bougher, S. Graham, T. D. Baratunde A. Cola, M.-H. Ji, J. Kim, R. Dupuis, W. Lv, and A. Henry, Rethinking phonons: The issue of disorder,

- npj Computational Materials **3**, 49 (2017).
- [42] J. L. Feldman, P. B. Allen, and S. R. Bickham, Numerical study of low-frequency vibrations in amorphous silicon, *Phys. Rev. B* **59**, 3551 (1999).
  - [43] R. W. Gurney, Lattice vibrations in graphite, *Phys. Rev.* **88**, 465 (1952).
  - [44] P. B. Sherry and C. A. Coulson, The vibrational frequency distribution of graphite: I. out-of-plane modes of a single layer, *Proceedings of the Physical Society. Section B* **69**, 1326 (1956).
  - [45] G. F. Newell, Vibration spectrum of graphite and boron nitride. ii. the three-dimensional spectrum, *The Journal of Chemical Physics* **27**, 240 (1957), <https://doi.org/10.1063/1.1743680>.
  - [46] C. H. Lui, L. M. Malard, S. Kim, G. Lantz, F. E. Laverge, R. Saito, and T. F. Heinz, Observation of layer-breathing mode vibrations in few-layer graphene through combination raman scattering, *Nano Letters* **12**, 5539 (2012), pMID: 22963681, <https://doi.org/10.1021/nl302450s>.
  - [47] H. R. Seyf, W. Lv, A. Rohskopf, and A. Henry, The importance of phonons with negative phase quotient in disordered solids, *Scientific reports* **8**, 2627 (2018).
  - [48] D. Surblys, H. Matsubara, G. Kikugawa, and T. Ohara, Methodology and meaning of computing heat flux via atomic stress in systems with constraint dynamics, *Journal of Applied Physics* **130**, 215104 (2021), <https://doi.org/10.1063/5.0070930>.
  - [49] D. Surblys, H. Matsubara, G. Kikugawa, and T. Ohara, Application of atomic stress to compute heat flux via molecular dynamics for systems with many-body interactions, *Phys. Rev. E* **99**, 051301 (2019).
  - [50] M. S. Green, Markoff random processes and the statistical mechanics of time-dependent phenomena. ii. irreversible processes in fluids, *The Journal of Chemical Physics* **22**, 398 (1954), <https://doi.org/10.1063/1.1740082>.
  - [51] R. Kubo, M. Yokota, and S. Nakajima, Statistical-mechanical theory of irreversible processes. ii. response to thermal disturbance, *Journal of the Physical Society of Japan* **12**, 1203 (1957), <https://doi.org/10.1143/JPSJ.12.1203>.
  - [52] S. Nosé, A molecular dynamics method for simulations in the canonical ensemble, *Molecular Physics* **52**, 255 (1984), <https://doi.org/10.1080/00268978400101201>.
  - [53] W. G. Hoover, Canonical dynamics: Equilibrium phase-space distributions, *Phys. Rev. A* **31**, 1695 (1985).
  - [54] P. B. Allen and J. L. Feldman, Thermal conductivity of glasses: Theory and application to amorphous si, *Phys. Rev. Lett.* **62**, 645 (1989).
  - [55] C. Y. Ho, R. W. Powell, and P. E. Liley, Thermal conductivity of the elements, *Journal of Physical and Chemical Reference Data* **1**, 279 (1972), <https://doi.org/10.1063/1.3253100>.
  - [56] A. Stukowski, Visualization and analysis of atomistic simulation data with OVITO—the open visualization tool, *Modelling and Simulation in Materials Science and Engineering* **18**, 015012 (2009).
  - [57] Jmol: an open-source Java viewer for chemical structures in 3D.



# Supplementary Material: Atomistic Nature of Amorphous Graphite

C. Ugwumadu,<sup>1,\*</sup> K. Nepal,<sup>1</sup> R. Thapa,<sup>1</sup> and D. A. Drabold<sup>1</sup>

<sup>1</sup>*Department of Physics and Astronomy,  
Nanoscale and Quantum Phenomena Institute (NQPI),  
Ohio University, Athens, Ohio 45701, USA*

(Dated: August 31, 2022)

## Sect. S1. Description of Animations produced for the amorphous Graphen (aG) models

We have produced some animations to aid the reader in visualizing some of the discussions in the paper. The animations can be found [here](https://people.ohio.edu/drabold/kent_movies/) or by visiting the url: [https://people.ohio.edu/drabold/kent\\_movies/](https://people.ohio.edu/drabold/kent_movies/)  
The descriptions for the video files are as follows:

1. **aG\_Formation.mp4**: This describes the formation process of aG.
2. **high\_freq.mp4**: This shows the vibration in aG at the high-frequency end of the spectrum, where the localization is on pentagon ring-forming atoms. Fig. S1 is a snapshot of one is such vibrations, the arrows in Fig. S1 (and subsequent animations) is a vector indicating the vibration path for the participating atoms. The animation show the vibration at a frequency of 2023.13 cm<sup>-1</sup>
3. **quasiLocalized\_freq.mp4**: This vibration has a mid-spectrum frequency of 745.32 cm<sup>-1</sup>. It shows the resonant modes in the vibrations of aG. We draw the reader's attention to the mixture of in-plane and out-of-plane vibrations at this frequency.
4. **low\_freq.mp4**: The animation show vibrations at the low-end frequency of 76.54 cm<sup>-1</sup> is shown in this animation. clearly, the vibrations are not localized and constitute mostly out-of-plane, "acoustic-like" vibrations

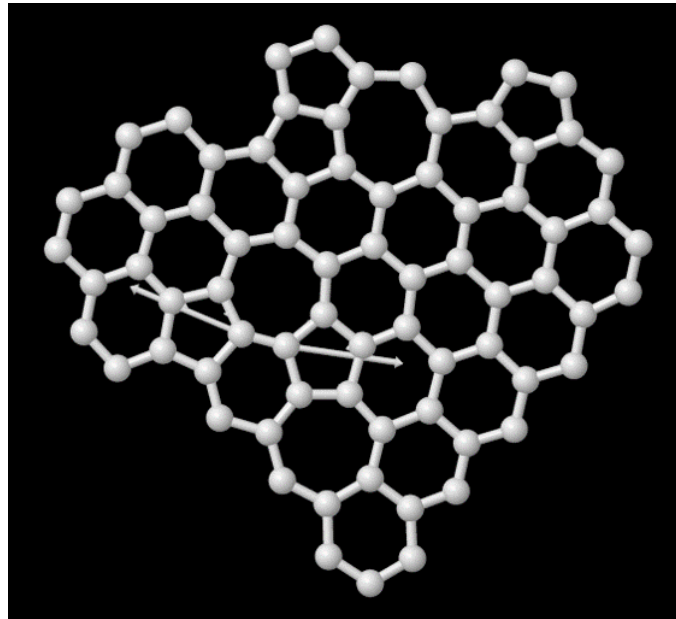


FIG. S1: Snapshot of a high-frequency vibration in aG. The arrows show the direction of motion for the participating atoms.

---

\* Corresponding author.  
E-mail: [cu884120@ohio.edu](mailto:cu884120@ohio.edu)